J. Fluid Mech. (2012), *vol.* 708, *pp.* 128–148. © Cambridge University Press 2012
doi:10.1017/jfm.2012.297

Agglomeration and de-agglomeration of rotating wet doublets

Carly M. Donahue, William M. Brewer, Robert H. Davis and Christine M. Hrenya†

Department of Chemical and Biological Engineering, University of Colorado, Boulder, CO 80309-0424, USA

(Received 16 December 2011; revised 11 June 2012; accepted 12 June 2012; first published online 21 August 2012)

In this work, experiments using a pendulum apparatus were conducted for two particles engaged in oblique, wetted collisions over a range of impact angles, impact velocities, coating thicknesses, liquid viscosities, particle materials, and particle radii. From previous studies on normal or head-on collisions, the two particles bounce apart if the Stokes number (a ratio of particle inertia to viscous forces) exceeds a critical value, whereas they stick together if the Stokes number is below this critical value. However, for oblique collisions, an additional outcome is observed at moderate Stokes numbers and impact angles, in which the spheres initially stick together, rotate as a doublet, and then separate due to centrifugal forces. We refer to this outcome as 'stick–rotate–separate'. For subcritical Stokes numbers exhibiting this new outcome, the experimental results for the apparent coefficient of normal restitution and angle of rotation from impact to separation show only weak dependence on the fluid viscosity and thickness and the dry restitution coefficient, whereas they both decrease with increasing particle radius. These results are in contrast with those for supercritical Stokes numbers in which the spheres bounce upon impact. An accompanying theory based on lubrication forces, the glass transition of the liquid layer, and solid deformation and rebound agrees well with experimental results and gives insight into the observed trends.

Key words: granular media, lubrication theory, particle/fluid flow

1. Introduction

Collisions between wetted (liquid-coated) particles are observed in a plethora of systems in nature such as pollen capture and avalanches, and in industrial operations such as granulation, pneumatic transport and drying of wetted particles. The liquid coatings cause cohesive forces, which influence particle-level interactions and macroscopic properties of wet-particle systems. In wetted systems, forces between particles can be categorized as capillary (static) forces or viscous (dynamic) forces. The focus of this work is on the latter.

Experiments on macroscopic (bulk) flow of wetted particles (Lekhal *et al.* 2006; Xu, Orpe & Kudrolli 2007; Liu, Yang & Yu 2011) have been conducted to examine ability to flow, the formation of agglomerates, etc. and have revealed interesting trends such as the relationship between particle segregation and liquid-bridge formation.

† Email address for correspondence: hrenya@colorado.edu

https://doi.org/10.1017/jfm.2012.297 Published online by Cambridge University Press

One common method to further understand the experimental observations is through discrete element method (DEM) simulations (Mikami, Kamiya & Horio 1998; Talu, Tardos & Khan 2000; Li & McCarthy 2005; Chaudhuri *et al.* 2006; Weber & Hrenya 2006; Kantak, Hrenya & Davis 2009). The DEM contains microscopic (particle-level) descriptions of the inter-particle forces due to the liquid bridge between particles, though more have focused on the capillary (static) forces than on the viscous (dynamic) forces. Another way to model macroscopic flows is through population (continuum) balances, which describe agglomeration processes via a rate equation (Iveson 2002). For both DEM simulations and population balances, accurate models of the microscopic forces are required for good predictions. Previous theoretical studies have produced expressions for the capillary force between two particles connected by a bridge that agree well with experimental measurements (Fisher 1926; Mason & Clark 1965; Cross & Picknett 1968; Lian, Thornton & Adams 1993). On the other hand, theories to describe the viscous force at the particle level, particularly the agglomeration/de-agglomeration behaviour, are relatively limited.

In this work, a microscopic approach is taken to investigate wetted collisions between two particles in which viscous (dynamic) forces dominate over capillary (static) forces, and the liquid flow is in the low-Reynolds-number regime. Consequently, Stokes flow prevails and the normal Stokes number,

$$St_n = mv_{0,n}/6\pi\mu a^2, \tag{1.1}$$

has been found to be a key dimensionless parameter (Davis, Serayssol & Hinch 1986; Lian, Adams & Thornton 1996). Here, $m = m_1m_2/(m_1 + m_2)$ is the reduced mass, $v_{0,n}$ is the normal component of the relative impact velocity, μ is the liquid viscosity, and $a = a_1a_2/(a_1 + a_2)$ is the reduced radius, where the subscripts 1 and 2 refer to particles 1 and 2, respectively. For normal collisions, de-agglomeration or rebound of colliding particles occurs for values of St_n greater than a critical Stokes number, namely St_n^*. The value of St_n^* can be determined either empirically via experiments or theoretically by considering the properties of both the fluid and the solid particles (Ennis, Tardos & Pfeffer 1991; Davis, Rager & Good 2002; Donahue, Hrenya & Davis 2010*a*). Recent experiments on normal collisions between a particle and a wetted wall have verified the lubrication force for $St_n < St_n^*$ (Marston, Wong & Thoroddsen 2010). In immersed collisions dominated by Stokes flow, velocity reversal of a particle impacting on a wall occurs when St_n is greater than a critical value of Stokes number, St_n^*, approximately equal to 10 (Joseph *et al.* 2001; Gondret, Lance & Petit 2002) for both normal and oblique collisions. Experiments on wetted particle–wall oblique collisions have shown that, for a range of St_n greater than St_n^*, the normal and tangential motions are approximately decoupled, which suggests that the value of St_n^* found in head-on collisions might also demarcate agglomeration versus de-agglomeration in oblique collisions (Kantak & Davis 2004). However, the ability of St_n^* to predict agglomeration versus de-agglomeration in oblique collisions was not verified due to experimental limitations.

Unlike previous efforts, here we investigate oblique collisions between a dry particle and a wetted particle (the theory also applies to oblique collisions between two wetted particles, while the experiments would need minor modification for both particles to be wetted prior to collision). Experiments are performed using a pendulum apparatus and are compared to theoretical predictions. In contrast to oblique, particle–wall collisions, the target is now mobile, such that an agglomerated doublet (connected by a liquid bridge) can form and rotate. Recently, we observed a new outcome for oblique, particle–particle collisions in which two colliding particles initially form an

https://doi.org/10.1017/jfm.2012.297 Published online by Cambridge University Press

agglomerate and then later de-agglomerate due to centrifugal forces (Donahue *et al.* 2012). In that work, a corresponding theory was developed that agrees well with the regime map of outcomes for impact angle versus St_n, and both experiments and predictions show that the new outcome occurs at large impact angles for $St_n < St_n^*$. Here, we expand the range of parameters to different liquid viscosities, coating thicknesses, particle materials and particle radii and analyse the corresponding trends of the (wet) normal restitution coefficient and rotation angle. Surprisingly, the trends depend on whether a de-agglomerating collision occurs for $St_n > St_n^*$ or $St_n < St_n^*$. Furthermore, the theory established in Donahue *et al.* (2012) is able to predict the trends and provides further insight into the physical mechanisms responsible for particle reversal and de-agglomeration.

2. Experimental setup

The experimental setup is composed of two solid spheres suspended with pendulum strings of 1 m length, as shown in figure 1. The pendulums strings are attached from above to a rotating glass plate. The string holding the striker is attached to the centre of the plate, so that when the plate is rotated its position does not change (figure 1*b*). The string holding the target particle is attached one particle diameter away from the striker string. As the plate is rotated, the position of the target particle moves relative to the striker such that a range of impact angles is possible (figure 1*c*). Prior to the collision, the striker particle is held in place by a gate that employs a solenoid as the release mechanism. The position of the gate can be moved along the track to achieve different impact velocities. The gate cradles the particle (figure 1*b*) for accurate positioning and to ensure minimal rotational motion is imparted to the striker. The target particle is coated with silicon oil, which is contained in a bath positioned underneath the target particle. The bath lifts to coat the particle, and the time that the liquid is allowed to drip from the particle prior to collision determines the thickness of the liquid coating at collision.

2.1. *Materials*

The pendulum string is attached to the particles via a small tube welded on the top of the particle. The string is ice fishing line manufactured by Berkley, chosen for its high spring constant (stiff) of 1.2 kN m^{-1}, which balances the centrifugal acceleration of the striker particle as it swings through an arc before it collides with the stationary target particle. The particles are either chrome steel (AISI 52100) or stainless steel (316 grade). The properties of the chrome-steel particles are: dry restitution coefficient $e_{dry} = 0.99$; Young's modulus $E = 2.03 \times 10^{11}$ N m^{-2}; Poisson's ratio $\upsilon = 0.28$; density $\rho = 7830$ kg m^{-3}; reduced radius $a = 6.4$ or 4.0 mm. The properties of the stainless-steel particles are: dry restitution coefficient $e_{dry} = 0.90$; Young's modulus $E = 1.93 \times 10^{11}$ N m^{-2}; Poisson's ratio $\upsilon = 0.35$; density $\rho = 8030$ kg m^{-3}; reduced radius $a = 6.4$ mm. The particles are coated with oil of viscosities 5.1, 12, or 99 Pa s at 25 °C, which is the nominal temperature of the experiments, and all three oils have densities of 0.97 g cm^{-3}. The oil is a general-purpose, silicone fluid manufactured by Brookfield Engineering Laboratories. To summarize the properties, a list of the collisional parameters can be found in table 1. The notation used to describe each case refers to viscosity, namely low (μ_{low}), medium (μ_{med}), or high (μ_{high}); coating thickness, namely small layer ($x_{0,small}$), medium layer ($x_{0,med}$), large layer ($x_{0,large}$), or extra-large layer ($x_{0,xlarge}$); particle material, namely chrome steel (cs) or stainless steel (ss); and particle radius, namely large (a_{large}) or small (a_{small}).

https://doi.org/10.1017/jfm.2012.297 Published online by Cambridge University Press

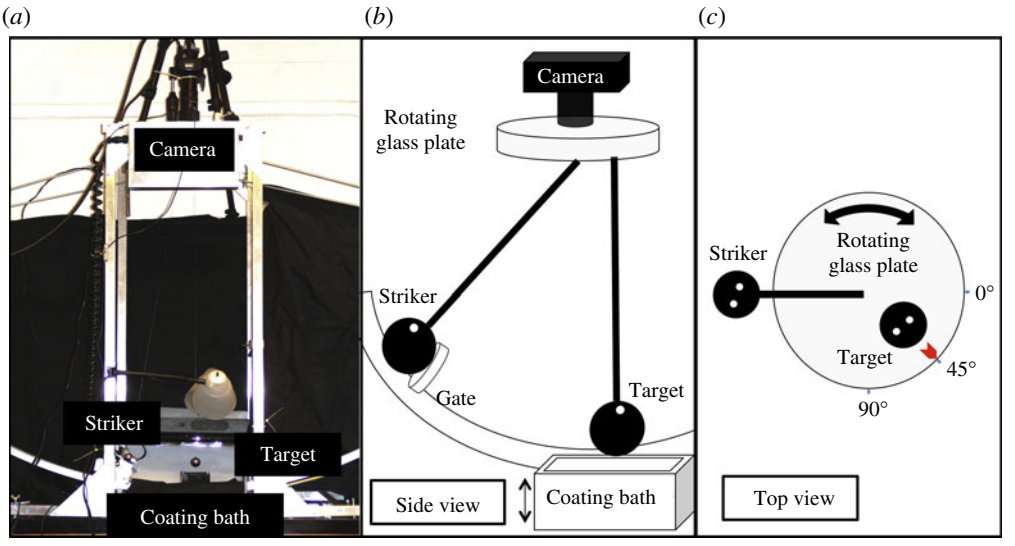


FIGURE 1. (Colour online) Experimental setup: schematic of (*a*) the side view of the pendulum apparatus; (*b*) the release mechanism; and (*c*) top view of the pendulum apparatus.

Case	Liquid viscosity (Pa s)	Coating thickness (μm)	Steel particle material	Particle radius (mm)
$\mu_{low}_x_{0,med}_ss_a_{large}$	5.12	270	Stainless	12.7
$\mu_{low}_x_{0,small}_ss_a_{large}$	5.12	180	Stainless	12.7
$\mu_{med}_x_{0,med}_cs_a_{small}$	12.0	263	Chrome	7.9
$\mu_{med}_x_{0,large}_cs_a_{large}$	12.0	418	Chrome	12.7
$\mu_{med}_x_{0,large}_ss_a_{large}$	12.0	420	Stainless	12.7
$\mu_{med}_x_{0,med}_cs_a_{large}$	12.0	270	Chrome	12.7
$\mu_{med}_x_{0,med}_ss_a_{large}$	12.0	270	Stainless	12.7
$\mu_{high}_x_{0,large}_ss_a_{large}$	99.0	850	Stainless	12.7

TABLE 1. Experimental parameters.

2.2. *Methods*

To characterize the collisions, two sets of measurements are performed: (i) off-line measurements of the thickness of the liquid layer coating the target particle; and (ii) on-line measurement of pre- and post-collisional velocities (translational and rotational) and impact angle. First, measurements of the coating thickness are made independently from the collisions with a high-resolution Pentax SLR K110D with 6.1 megapixels. Wide-angle distortion is minimized using a zoom lens that allows the camera to be placed approximately 1.5 m away from the coated particle. Photographs are taken every 3 s during the dripping process, and the process is repeated five times. The lighting, aperture, and shutter speed are set at levels to make the particle, and particularly the edge of the particle, well defined and dark with respect to the background. The photographs are analysed in *Matlab*, and the coating thickness is found from a given photograph by subtracting the edge-to-edge distance of the dry-

https://doi.org/10.1017/jfm.2012.297 Published online by Cambridge University Press

particle photograph from the wet particle, and then dividing the resulting quantity by 2. The coating thickness is then found for a particular drip time from a linear fit of these off-line data 5 s before and after the drip time. The error in the measurements of the coating thickness is approximately ± 5 μm.

Second, the particle positions, and hence the relevant velocities and geometries, are tracked in time throughout the collisional process using a high-speed camera that is placed above the rotating glass plate. The camera is manufactured by DVC (model 340 M) with a 640×480 pixel resolution. However, depending on the impact velocity and angle, the effective resolution ranges between approximately 200×75 and 400×175 pixels. Similar to the high-resolution camera, a Navitar 7000 zoom lens allows the camera to be placed approximately 1 m from the particles, so that wide-angle effects are essentially eliminated. The camera operates at 40 MHz with a frame rate of 250 and 400 Hz depending on the resolution. Two fluorescent dots are painted on the top of each particle, and the apparatus is lit using fluorescent lights only. In this way, the camera tracks only the dots, so that linear and angular velocities and the impact angle can be extracted using image tools in *Matlab*. Depending on the impact angle and the impact velocity, the translational-velocity error ranges between 0.010 and 0.023 m s^{-1}, the rotational-velocity error ranges between 0.006 and 0.015 rad s^{-1}, and the impact-angle error ranges between 0.9°and 6.2°. Each pixel is between 300 and 360 μm, depending on the focus of the camera. The two particles are considered to be separated when they reach a separation distance of three pixels. This distance was the minimum distance at which the outcomes determined by this criterion are consistent with the outcomes observed via visual inspection. Furthermore, the rotation angle is weakly dependent on this criterion.

3. Theory description

To illuminate the dominant physical mechanisms, the theory from Donahue *et al.* (2012) for two-particle, wetted, oblique collisions is used. In addition to the typical fluid forces, tension from the pendulum strings is included. As the doublet rotates from its impacting position, tension from strings arises that resist normal and rotational motion. The relevant dimensionless numbers are the Reynolds number Re, and the capillary number Ca. The largest Reynolds number (ratio of fluid inertia to fluid viscous forces in the liquid gap between colliding particles) encountered experimentally is

$$Re_{max} = \rho v_{0,n} x_0 / \mu = 0.04, \tag{3.1}$$

where ρ is the liquid density, $v_{0,n} = v_0 \cos\theta_0$ is the initial normal component of relative velocity between particles, θ is the angle between the relative velocity and the line connecting the centres of the particles at initial contact and the subscript 0 indicates the initial impact value, x_0 is the initial coating thickness, and μ is the liquid viscosity (figure 2). Therefore, the collisions occur at low Re, and the dynamics of the liquid between the particles is governed by Stokes flow (lubrication). The smallest capillary number (ratio of viscous forces in the liquid gap between the particles to capillary forces between the particles) encountered is

$$Ca_{min} = 3\mu a v_{0,n} / \sigma x_0 = 1500, \tag{3.2}$$

where σ is the surface tension of the silicon oil. Since $Ca \gg 1$, capillary forces are negligible, as was confirmed by Salcudean *et al.* (2009). Finally, an evaluation of the Stokes number for a particle suspended in air shows that resistance from the interstitial air is negligible.

https://doi.org/10.1017/jfm.2012.297 Published online by Cambridge University Press

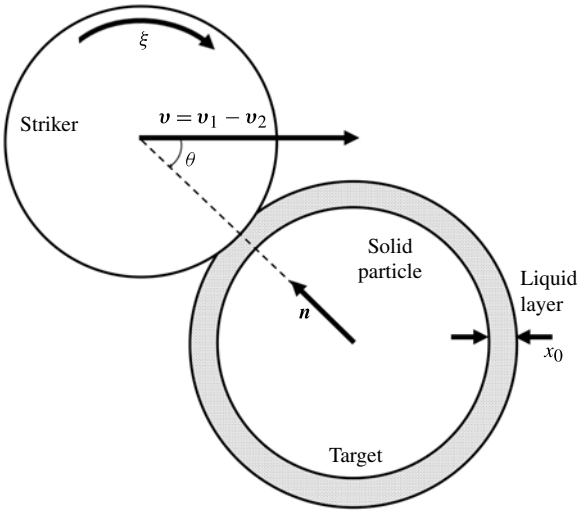


FIGURE 2. Impact geometry.

3.1. *Lubrication*

The viscous (lubrication) force that resists the relative motion of the particles acts in both the normal and the tangential directions. For small deformations and for $x \ll a$, the normal component of the lubrication force has been derived by Kantak & Davis (2006) for liquid-coated spheres as

$$F_{L,n} = \frac{6\pi\mu a^2 v_n}{x}\left(1 - \frac{x}{x_0}\right)^2, \tag{3.3}$$

where the subscript n indicates the normal direction. The normal vector, $\boldsymbol{n}$, is a unit vector that points from the centre of the target to the centre of the striker (figure 2). In the tangential direction, the force between two immersed particles was solved numerically by O'Neill & Majumdar (1970) such that

$$F_{L,t} = -24\pi\mu a^2\left(\frac{1}{3}\ln\frac{2a}{x_0}(\omega - \xi) + 1.2720\omega + 0.1583\xi\right), \tag{3.4}$$

where $\omega = (v/4a)\sin\theta$ is the angular velocity of the doublet about the centre of mass of the doublet, ξ is the angular velocity of each single particle about its centre of mass (i.e. rotational velocity of particle), and the subscript t indicates the tangential direction (figure 2). Here, we restrict our model to rotation about an axis normal to the plane of motion, so that the motion of the two spheres during collision is constrained to a single (horizontal) plane. In this work, the particles are wetted rather than immersed; therefore, the second and third terms on the right-hand side of (3.4) are omitted since they are due to the viscous resistance from the liquid in the outer region (absent for wetted particles) away from the liquid gap between the particles. Since both particles initially do not rotate about their centres ($\xi_{striker} = \xi_{target} = 0$) and the fluid exerts an equal-magnitude force on each particle, the corresponding angular accelerations of the two identical particles are also equal; therefore, throughout the collision the particles have equal angular velocities ($\xi_{striker} = \xi_{target} = \xi$). Finally, when $\omega = \xi$, the surfaces of the particles do not move relative to each other and thus there is no shearing of the fluid between the particles (i.e. $F_{L,t} = 0$).

https://doi.org/10.1017/jfm.2012.297 Published online by Cambridge University Press

3.2. *String tension*

To accurately model the experiments, the force of tension from the pendulum strings must be accounted for. In particular, at the moment the striker particle collides with the target particle, tension only acts in the vertical direction parallel to gravity; therefore, string tension does not influence the collision at the moment of impact (i.e. tension is balanced by gravitational force). However, as the particles begin to rotate about the centre of mass of the doublet, the pendulum strings are no longer aligned with gravity. Consequently, tension from the pendulum strings emerges in both the normal and tangential directions. In the normal direction, this tension is

$$F_{S,n} = \frac{8mga}{\ell}\sin^2\left(\frac{\beta}{2}\right)\sqrt{1-\frac{16a^2}{\ell^2}\sin^2\left(\frac{\beta}{2}\right)}, \tag{3.5}$$

where g is the acceleration due to gravity, ℓ is the length of the pendulum string, and β is the angle the doublet has rotated from the time of the initial impact. In the tangential direction, the tension from the strings is

$$F_{S,t} = -\frac{4mga}{\ell}\sin(\beta)\sqrt{1-\frac{16a^2}{\ell^2}\sin^2\left(\frac{\beta}{2}\right)}. \tag{3.6}$$

3.3. *Kinematic equations*

The kinematic equations corresponding to the experimental setup are

$$\frac{\mathrm{d}x}{\mathrm{d}t} = -v_n, \tag{3.7}$$

$$m\frac{\mathrm{d}v_n}{\mathrm{d}t} = F_{L,n} + F_{S,n} - 4ma\omega^2, \tag{3.8}$$

$$\frac{\mathrm{d}\beta}{\mathrm{d}t} = \omega, \tag{3.9}$$

$$4ma\frac{\mathrm{d}\omega}{\mathrm{d}t} = F_{L,t} + F_{S,t} + 2mv_n\omega, \tag{3.10}$$

$$\frac{8}{5}ma\frac{\mathrm{d}\xi}{\mathrm{d}t} = -F_{L,t}. \tag{3.11}$$

Equations (3.7)–(3.11), together with expressions given above for the lubrication and tension forces (equations (3.3)–(3.6)), are solved in time for x, β, v_n, ω and ξ. The particles approach each other with an initial separation equal to the initial (measured) coating thickness x_0 (equation (3.3)), normal impact velocity $v_{n,0} = v_0\cos\theta_0$, initial angular velocity of the agglomerate $\omega_0 = v_0\sin\theta_0/(4a)$, and initial angular velocity of each particle $\xi_0 = 0$. If the initial angular velocity for either particle is not zero, then a slightly more complicated analysis would be required, with (3.4) and (3.11) modified to account for the rotation of each particle. Upon approach, the particles may stick (agglomerate) if their normal relative acceleration and velocity drop to zero. During the collisional process, the particles may reverse direction due to: (i) centrifugal forces; or (ii) encountering a reversal criterion also present in normal collisions (i.e. glass transition of liquid layer, elastohydrodynamics, or surface roughness), which is discussed in more detail below (§ 3.4). As the particles move away from each other, they may stick (agglomerate) if their normal acceleration and velocity drops to zero due to viscous resistance. Otherwise, de-agglomeration is said to occur when their separation distance reaches x_0. Additionally, the simulations are stopped and are considered to stick (agglomerate) if the doublet rotates 180° from its initial position (at

https://doi.org/10.1017/jfm.2012.297 Published online by Cambridge University Press

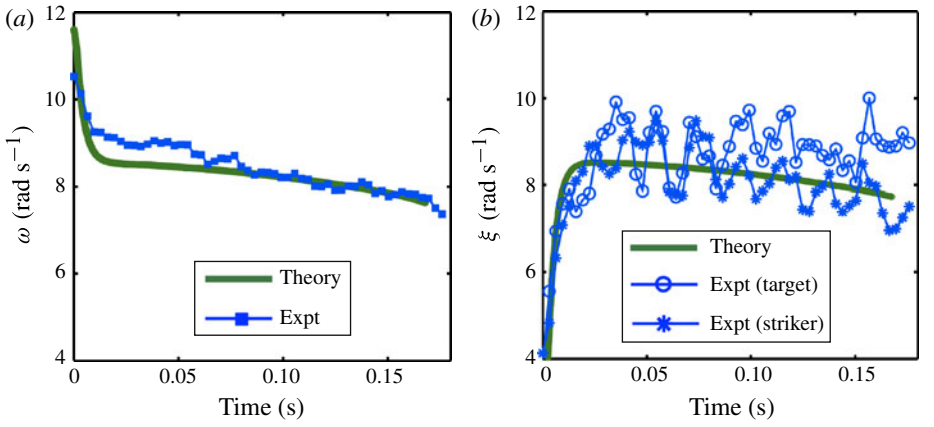


FIGURE 3. (Colour online) Experimental results and theoretical predictions of the angular velocity of (*a*) a doublet (ω) and (*b*) particles (ξ) over time for a collision of case $\mu_{med}_x_{0,thick}_cs_a_{large}$ for $St_n = 1.1$ and $\theta_0 = 46°$. The initial, rapid decline of the doublet angular velocity over short times ($t <\sim 0.01$ s) is due to the tangential lubrication force, while the slower decline at longer times is due to the string tension.

which point the strings cross) or if the angular velocity of the doublet reverses before a separation distance equal to x_0 is achieved.

To assess the accuracy of the theory, predictions of the angular velocity of the doublet (ω) and the angular velocity of the particles (ξ) over time are compared to experimental results in figure 3. The error in ω is generally smaller than the error in ξ, since two sets of two dots painted on the top of each particle spaced further apart are used to determine ω, whereas only one set of dots is used to find ξ. As mentioned previously, when $\omega = \xi$ (time $\sim$0.01 s), the surfaces of the particles no longer rotate relative to each other, and the doublet has formed an approximately rigid dumbbell. The initial rapid decline in ? and the corresponding rapid increase in ξ over this short time is due to the tangential lubrication as the doublet quickly forms a dumbbell. At longer times, the relatively slow decline in ω and ξ results from string tension. As mentioned previously, the tangential lubrication theory used here is a modified version of that for two immersed spheres; since the results for the conditions in figure 3 are representative of the rest of the parameter space, the modified immersed theory serves as a good approximation for wetted particles.

3.4. *Reversal criteria*

As stated previously, when the particles approach each other for normal (head-on) collisions, three mechanisms have been identified that cause the particles to deform and then reverse their relative motion: (i) glass transition of the liquid; (ii) elastohydrodynamic forces; and (iii) particle roughness. First, the pressure in the liquid gap rapidly increases during approach; if the pressure exceeds the glass-transition pressure, p_{gt}, then the liquid behaves as a solid and the particles reverse direction. The glass-transition rebound separation is

$$x_{gt} = \sqrt{\frac{3\mu a v_n x_0^2}{(p_{gt} - p_{atm})\, x_0^2 + 3\mu a v_n}} \approx \sqrt{\frac{3\mu a v_n}{(p_{gt} - p_{atm})}} \quad \text{when } x_{gt} \ll x_0, \tag{3.12}$$

https://doi.org/10.1017/jfm.2012.297 Published online by Cambridge University Press

where p_{atm} is the atmospheric pressure (Donahue *et al.* 2010*b*). The glass transition can be viewed as a limiting case of non-Newtonian behaviour, wherein the effective viscosity of the liquid film becomes very large at very high compressive pressures (Barnocky & Davis 1989). In recent work, Marston *et al.* (2010) have shown that a different non-Newtonian effect due to shear thinning in the thin liquid layer for certain fluids can also affect rebound. Second, the large lubrication pressures cause the solid particle to deform; the stored energy in this deformation leads to reversal in the relative normal motion if the following separation length scale, determined using a coupling of elastic and lubrication theories (i.e. elastohyrdrodynamics), is reached:

$$x_r = (6\pi\Theta\mu a^{3/2} v_n/\sqrt{2})^{2/5}, \tag{3.13}$$

where $\Theta = 2(1-\upsilon^2)/\pi E^2$ and υ is Poisson's ratio and E is Young's modulus (Davis *et al.* 1986). Finally, the surface roughness, x_b, is assumed to be 1 μm based on previous measurements of similar materials (Barnocky & Davis 1988), and the particle surfaces will touch and the relative normal particle velocity will reverse if this separation is reached. If the theory predicts that any one of the three reversal criteria has been met upon approach (i.e. the gap x decreases to the largest of x_{gt}, x_r, or x_b), then the particles deform and rebound with their normal relative velocity reversed and multiplied by the dry restitution coefficient e_{dry} to account for the (kinetic) energy dissipation experienced by the particle during deformation.

To assess the accuracy of the new component of our theory (involving rotational motion of oblique collisions), it is essential to start with accurate predictions for normal (head-on) collisions. In previous work, the glass-transition rebound criterion dictated the reversal process for the conditions investigated and was critical in the prediction of the correct outcomes and trends for normal three-body collisions (Donahue *et al.* 2010*b*). In that three-body work, a pendulum apparatus was also used, and the materials and the range of parameters used were similar to this work. The theory used in Donahue *et al.* (2010*b*) is the same as in this work for head-on collisions with $\omega = \xi = 0$. Therefore, not surprisingly, the glass-transition state is the first reversal criterion met in the theoretical predictions here. In particular $x_{gt} > x_b$ and $x_{gt} > x_r$, because the steel spheres employed are relatively smooth and stiff. Due to a lack of well-established data for the value of p_{gt} for silicon oil, the value of p_{gt} has been chosen for each different viscosity oil used based on the experimental value obtained for St_n^*.

Figure 4 compares the normal wet restitution coefficient, $e_{w,n}$, found in experiments for normal collisions against the theoretical predictions. Since, for normal collisions, $e_{w,n}$ is a ratio of the magnitude of the relative post-collisional velocity to that of the pre-collisional velocity, $e_{w,n} = 0$ when the particles stick (agglomerate), and $e_{w,n} > 0$ when the particles bounce (de-agglomerate). Here, St_n increases due to an increase in impact velocity, as all other parameters remain unchanged. In figure 3, $St_n^* = 1.5$, representing the value of St_n at which $e_{w,n}$ transitions to a non-zero value. The current theoretical predictions agree well quantitatively and qualitatively with experimental results. Two other theories are also compared to experimental results. The theory of Kantak & Davis (2006) uses a complete treatment of elastohydrodynamics to model a wetted collision, but with constant viscosity. The theoretical predictions of Kantak & Davis (2006) have a somewhat fortuitous match of St_n^*, since not including the glass transition provides for closer approach and more resistance that balances the lack of (known) resistance upon rebound due to presumed cavitation; however, $e_{w,n}$ is underpredicted for $St_n > St_n^*$. The more simplified theory by Davis (1987), in

https://doi.org/10.1017/jfm.2012.297 Published online by Cambridge University Press

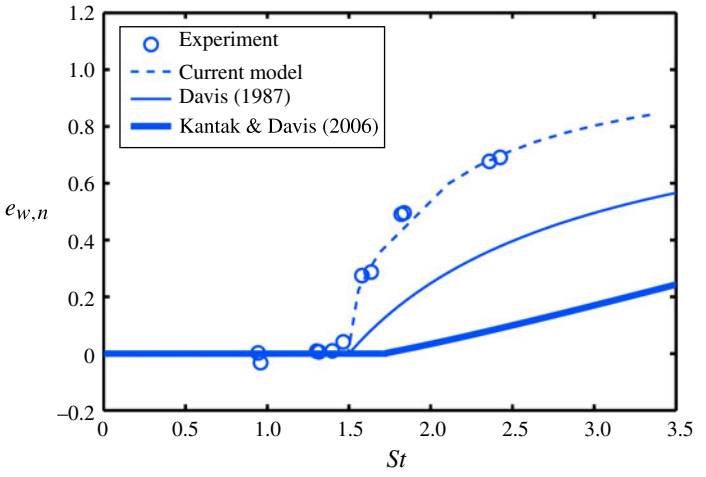


FIGURE 4. (Colour online) Restitution coefficient for normal (head-on) collisions for case $\mu_{med}_x_{0,large}_ss_a_{large}$ compared for the current theory, Davis (1987), and Kantak & Davis (2006).

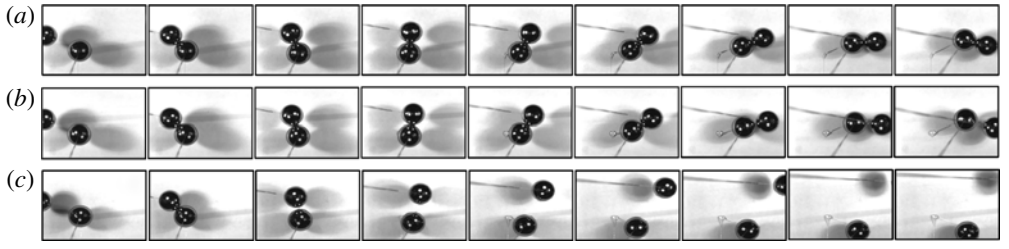


FIGURE 5. Top-view snapshots (using high-speed camera) of collisions with outcomes of (*a*) stick (S), (*b*) stick–rotate–separate (SRS), and (*c*) bounce (B) for parameters of case $\mu_{med}_x_{0,large}_cs_a_{large}$ and $\theta_0 = 45°$. Only the normal impact velocity was changed between the three subfigures, such that the impact velocities are: (*a*) 0.25 m s^{-1} ($St_n = 0.95$); (*b*) 0.29 m s^{-1} ($St_n = 1.1$); and (*c*) 0.34 m s^{-1} ($St_n = 1.3$). The time between each frame is 20 ms, for each of these cases.

which particles only rebound due to surface roughness, has the simple form $St_n = e_{dry}(1 - St_n^*/St_n)$ for $St_n > St_n^*$, where $St_n^* = \ln(x_0/x_b)$. Here, x_b is chosen such that St_n^* matches the experimental value. Again, the theory underpredicts the value of $e_{w,n}$ for $St_n > St_n^*$. Compared to the other two theories that do not include the glass transition, the current theory is the appropriate choice for this work.

4. Results and discussion

In figure 5, three sets of collision snapshots with different outcomes are shown, with only the impact velocity changed between the three sets. Two of the outcomes were also observed in previous experimental works involving wetted normal particle–particle and oblique particle–wall systems, namely stick (S, figure 5*a*) in which the striker particle forms an agglomerate with the target object, and bounce (B, figure 5*c*) in which the striker collides with the target and essentially immediately separates (Kantak

https://doi.org/10.1017/jfm.2012.297 Published online by Cambridge University Press

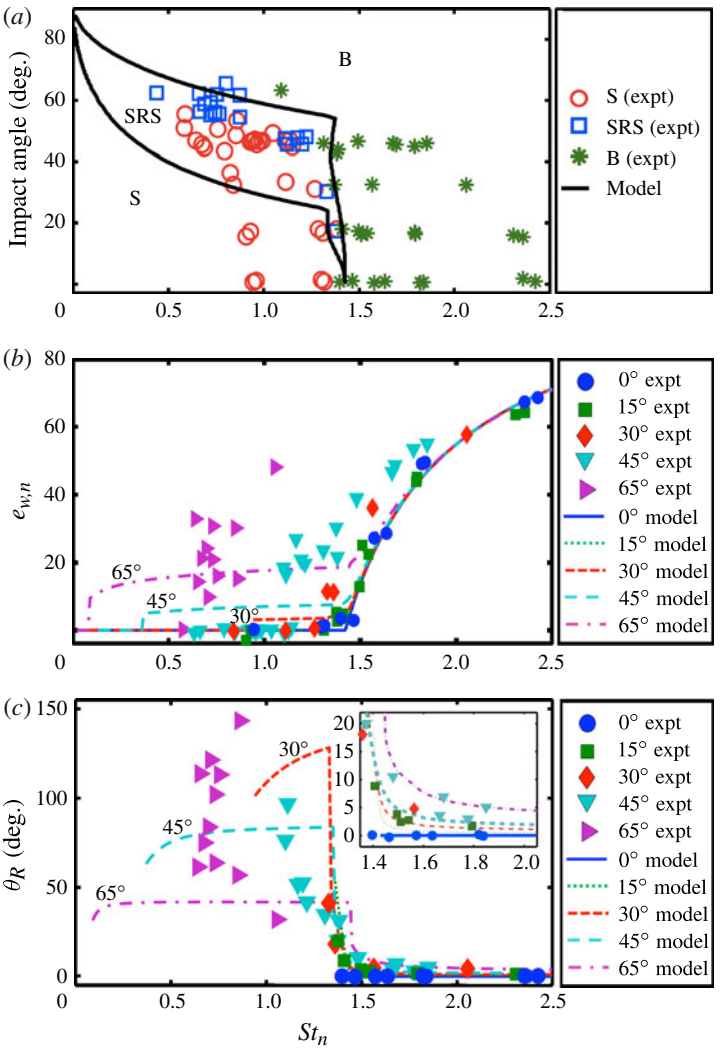


FIGURE 6. (Colour online) (*a*) Regime map of outcomes, (*b*) normal restitution coefficient and (*c*) rotation angle for case $\mu_{med}_x_{0,large}_cs_a_{large}$. The inset in (*c*) is a close-up of the theoretical predictions and experimental results in the vicinity of St_n^*.

& Davis 2004; Donahue *et al.* 2010*a*). The third outcome is only observed in oblique particle–particle collisions and is shown in figure 5(*b*) (Donahue *et al.* 2012). Here, the two particles collide and initially stick together, and then at a later time after the agglomerate has rotated through a significant angle, the two particles de-agglomerate due to centrifugal forces. This outcome, characterized by collisions that eventually separate but have collision durations greater than for head-on collisions, is named stick–rotate–separate (SRS).

As a first validation of the theory, figure 6 contains experimental data and theoretical predictions for case $\mu_{med}_x_{0,thick}_ss_a_{large}$. Figure 6(*a*) shows the regime map of outcomes over a range of impact angles and St_n. The symbols represent outcomes of individual experimental collisions (stick, stick–rotate–separate, and bounce), and the

https://doi.org/10.1017/jfm.2012.297 Published online by Cambridge University Press

lines represent the boundaries between the various outcomes predicted by the theory. The collision outcomes observed in the experiments show good agreement with the theoretical predictions, except that the observed impact angle that separates stick and stick–rotate–separate for a given St_n is higher than the predicted boundary. For normal collisions ($\theta_0 = 0°$), the Stokes number at the transition between stick and bounce, St_n^*, is equal to 1.4. For oblique collisions, experiments and theoretical predictions show generally that, if $St_n < St_n^*$, particles either stick or stick–rotate–separate, whereas if $St_n > St_n^*$, particles bounce. For $St_n < St_n^*$, sticking (S) occurs at small impact angles, while stick–rotate–separate (SRS) occurs at higher impact angles due to greater doublet rotational velocity and centrifugal forces. The boundary between stick and stick–rotate–separate for $St_n < St_n^*$ appears to be $\sim 20°$ higher in the experiments than for the theory, meaning that a large impact angle and, hence, a larger rotational velocity of the doublet after impact were required to achieve separation. A possible explanation is that fluid was drawn into the gap region by capillary forces during collision, thereby increasing the lubrication resistance to separation.

In collisions between dry particles, the normal restitution coefficient has traditionally been defined as $e_n = -(\boldsymbol{v}_f \cdot \boldsymbol{n}_0)/(\boldsymbol{v}_0 \cdot \boldsymbol{n}_0)$, where the subscripts 0 and f represent the initial and final values, respectively. This definition is sufficient for dry collisions, since the collision duration is short and particles do not rotate far; in other words, $\boldsymbol{n}$ does not vary significantly during the collision. But, when the particles do rotate significantly, as is true for sufficiently oblique collisions between wetted particles, so does the normal vector. Anomalous behaviour of the restitution coefficient due to the rotation of the colliding particles was first observed in nanocluster collisions reported by Saitoh *et al.* (2010). Therefore, in this work, a modified definition of the (wetted) normal restitution coefficient used is

$$e_n = -(\boldsymbol{v}_f \cdot \boldsymbol{n}_f)/(\boldsymbol{v}_0 \cdot \boldsymbol{n}_0). \tag{4.1}$$

Using this modified definition of the normal restitution coefficient, $e_{w,n}$ is plotted versus St_n in figure 6(*b*) for a range of impact angles. For each specified impact angle, symbols represent experimental collisions within 5° of the given angle, and curves represent the theoretical predictions. The theory agrees well with the experiment and correctly predicts the trend of $e_{w,n}$ as the impact angles changes. In particular, the curves of $e_{w,n}$ for impact angles of 15°and 30° are similar to the curve of the 0° collisions in both experiment and theory. Therefore, the small change in the value of $e_{w,n}$ at small impact angles indicates that centrifugal forces associated with the rotating pair play a negligible role in the de-agglomeration of these (nearly head-on) collisions. The curves of $e_{w,n}$ for larger impact angles of 45°and 65° show that collisions de-agglomerate ($e_{w,n} > 0$) for $St_n < St_n^*$ in both experiment and theory, and this de-agglomeration is the stick–rotate–separate (SRS) mechanism due to centrifugal forces. The corresponding predictions for $St_n > St_n^*$ are instead dominated by the same bounce (B) mechanisms that cause reversal in normal collisions, which is why they appear to collapse on the $\theta_0 = 0°$ curve. The discontinuity in the slope observed at St_n^* is due to the different mechanisms responsible for de-agglomeration for $St_n < St_N^*$ versus $St_n > St_n^*$. The scatter in measured $e_{w,n}$ increases as θ_0 increases, since the uncertainty in the measured θ_0 increases with θ_0 and more error is associated with the stick–rotate–separate outcome due to the sensitivity of rotation angle to impact velocity (figure 6*c*).

In addition to examining the normal components of motion, the rotational motion of an agglomerate is also investigated in terms of the rotation angle, θ_R, defined as the angle through which an agglomerate rotates between initial impact and

https://doi.org/10.1017/jfm.2012.297 Published online by Cambridge University Press

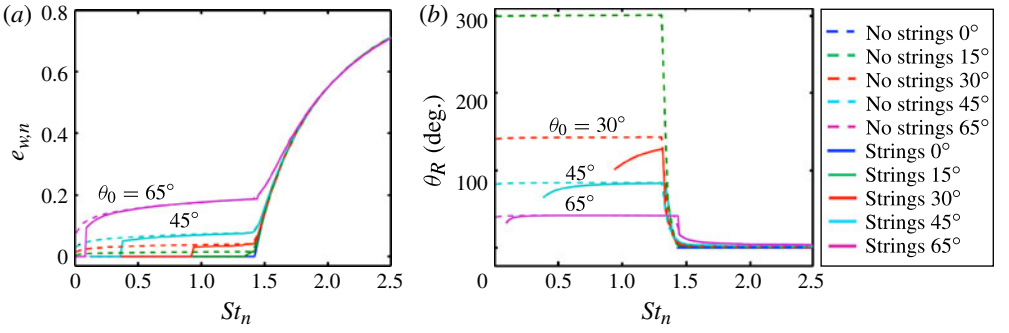


FIGURE 7. (Colour online) Theoretical predictions of (*a*) normal restitution coefficient and (*b*) angle rotated for case $\mu_{med}_x_{0,large}_cs_a_{large}$ at several impact angles with pendulum strings (solid curves) and without pendulum strings (dashed curves).

de-agglomeration:

$$\theta_R = \int_0^{t_c} \omega(t)\,\mathrm{d}t, \tag{4.2}$$

where t_c is the collision duration (i.e. the time during which the spheres are in near-contact with $x < x_0$ during the collision). Therefore, if either the collision duration or the doublet angular velocity ω increases, θ_R also increases. Figure 6(*c*) is a plot of θ_R versus St_n for those collisions that de-agglomerate (SRS and B). Near St_n^*, a sharp decrease in θ_R is observed for a given θ_0 in both experiment and theory as the outcome transitions from stick–rotate–separate to bounce. This observation stems from the fact that the collision duration of a stick–rotate–separate collision ($St_n < St_n^*$) is much longer than that of a bounce collision ($St_n > St_n^*$), allowing the particles to rotate further during the collision. Moreover, for $St_n > St_n^*$, θ_R increases as θ_0 increases for a given St_n in both experiment and theory, which is more clearly seen in the inset. In this region, the relative normal velocity of the particles reverses direction due to the normal reversal criteria (e.g. $x = x_{gt}$); therefore, the collision duration is short and primarily dependent on impact velocity (collision duration decreases as impact velocity increases) and not on θ_0. However, as θ_0 increases, the angular velocity of the agglomerate increases so that the particles rotate a larger distance in the same amount of time.

On the other hand, for $St_n < St_n^*$ the opposite trend is observed in figure 6(*c*); the rotation angle decreases as impact angle increases at fixed St_n in both experiment and theory. In this region, the centrifugal force is responsible for de-agglomeration, and the magnitude of the centrifugal force increases with impact angle in proportion to the square of the angular velocity. Therefore, the decrease in the collision duration due to increased centrifugal forces dominates over the increased angular velocity, and the particles do not rotate as far as θ_0 increases. While the theory predicts well the qualitative features of the experimental observations, a quantitative mismatch still persists. This quantitative mismatch may be due to the deformation of the liquid bridge as the particles move apart and liquid is pulled into the bridge.

The theory not only predicts the dynamics of the collisions, but, because it allows physical mechanisms to be turned 'on' and 'off', the influence of each factor can be ascertained. In figure 7, $e_{e,n}$ and θ_R are plotted both with string tension included and with string tension removed. Note that the values of $e_{w,n}$ and θ_R are largely unaffected

https://doi.org/10.1017/jfm.2012.297 Published online by Cambridge University Press

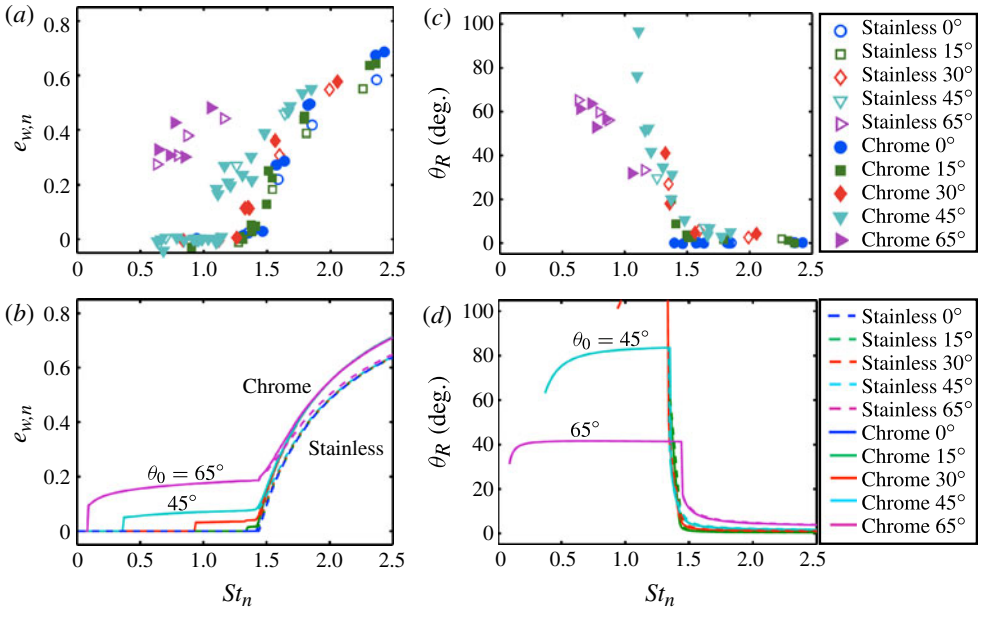


FIGURE 8. (Colour online) Normal restitution coefficient from (*a*) experiment and (*b*) theory, and rotation angle from (*c*) experiment and (*d*) theory as the dry restitution coefficient is increased from 0.90 (open symbols, dashed curves) to 0.99 (closed symbols, solid curves) for cases $\mu_{med}_x_{0,large}_cs_a_{large}$ and $\mu_{med}_x_{0,large}_ss_a_{large}$.

by turning off the string tension in regions where collisions had de-agglomerated with string tension (i.e. for $\theta_0 = 15°$, $St_n > 1.4$; for $\theta_0 = 30°$, $St_n > 1$; for $\theta_0 = 45°$, $St_n < 0.5$; and for $\theta_0 = 65°$, $St_n > 0.2$). Therefore, as described in the next section, the trends in $e_{w,n}$ and θ_R for de-agglomerating collisions are also not greatly affected by the presence of the pendulum strings. Except for one instance, string tension generally does not affect the observed trends in $e_{w,n}$ and θ_R for de-agglomerating collisions. However, for a given impact angle, the value of St_n that demarcates agglomeration versus de-agglomeration, $St^*(\theta_0)$, is largely influenced by string tension, since without string tension all oblique collisions are predicted to de-agglomerate (as also shown in Donahue *et al.* 2012); therefore, in this work the trends of $St^*(\theta_0)$ are not analysed. (In figure 7, with string tension, $St^*(\theta_0 = 0°) = 1.4$, $St^*(\theta_0 = 15°) = 1.3$, $St^*(\theta_0 = 30°) = 0.9$, $St^*(\theta_0 = 45°) = 0.4$, $St^*(\theta_0 = 65°) = 0.1$.)

4.1. *Effect of solid elasticity*

To determine the role of the elasticity of the solid sphere in a wetted collision, the cases $\mu_{med}_x_{0,large}_ss_a_{large}$ and $\mu_{med}_x_{0,large}_cs_a_{large}$ are compared so that only particle material changes from the softer stainless steel ($e_{dry} = 0.90$) to the harder chrome steel ($e_{dry} = 0.99$). Figure 8(*a*) is a plot of experimental values of $e_{w,n}$ versus St_n for a range of impact angles. Open and closed symbols represent stainless steel and chrome steel, respectively. The value of St_n^* (the critical St_n for de-agglomeration in head-on collisions) is not sensitive to e_{dry} and neither are the values of $e_{w,n}$ for $St_n < St_n^*$. However, for $St_n > St_n^*$, as e_{dry} is increased, the value of $e_{w,n}$ increases. Figure 8(*b*) shows the corresponding theoretical predictions. The experimental data and model curves are plotted on separate but adjacent graphs, so that the large numbers of data

https://doi.org/10.1017/jfm.2012.297 Published online by Cambridge University Press

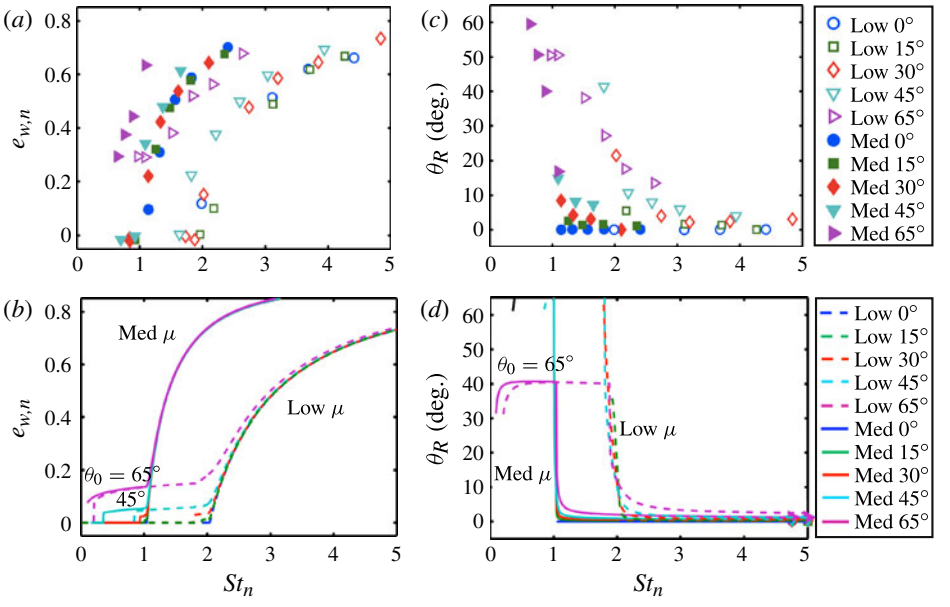


FIGURE 9. (Colour online) Normal restitution coefficient from (*a*) experiment and (*b*) theory, and rotation angle from (*c*) experiment and (*d*) theory as viscosity is increased from 5 Pa s (open symbols, dashed curves) to 12 Pa s (closed symbols, solid curves) for cases $\mu_{low}_x_{0,med}_ss_a_{large}$ and $\mu_{med}_x_{0,med}_ss_a_{large}$.

symbols do not obscure the trends shown by the theory curves. The theory agrees well with the experimental trends of $e_{w,n}$, though there are quantitative differences as noted earlier. The theory is especially useful here to provide insight into the cause of this trend. In particular, the value e_{dry} only affects the theoretical predictions if $St_n > St_n^*$ and bouncing occurs. Then, one of the three normal reversal criteria is met, and the relative velocity at that point is reversed and multiplied by e_{dry} to account for the dissipation of energy in the solid particle during deformation. However, when $St_n < St_n^*$, and the particles reverse direction due to centrifugal forces, they do not deform and the value of e_{dry} is not used.

To see how e_{dry} affects the rotational motion of the doublet, the experimental θ_R is plotted versus St_n in figure 8(*c*), and no difference in θ_R is noted between the two values of e_{dry} examined. Since the values of e_{dry} vary by only a small amount ($<10\,\%$), the collision duration negligibly decreases as e_{dry} increases. Furthermore, the particle material does not affect the angular velocity (equations (3.10) and (3.11)). Since collision duration and angular velocity are unaffected by e_{dry}, θ_R also does not depend on e_{dry}. The theory is able to correctly predict the trends, though it does exhibit some quantitative mismatch (figure 8*d*).

4.2. *Effect of liquid viscosity*

To investigate the effect of liquid viscosity, the cases $\mu_{low}_x_{0,med}_ss_a_{large}$ and $\mu_{med}_x_{0,med}_ss_a_{large}$, in which only the viscosity changes, are compared. Figures 9(*a*) and 9(*b*) are plots of $e_{w,n}$ versus St_n for the experiments and theoretical predictions, respectively. Both experiment and theoretical predictions show St_n^* decreases as viscosity increases (the particles more readily bounce at fixed St_n, which requires

https://doi.org/10.1017/jfm.2012.297 Published online by Cambridge University Press

larger impact velocity for larger viscosity). For the low-viscosity-oil collisions, $St_n^* \sim 2.0$, whereas for medium-viscosity-oil collisions, $St_n^* \sim 1.0$ (figure 9*a*).

In figure 9(*a*,*b*), for $St_n > 2.0$ (low-viscosity $St_n^* = 2.0$), as viscosity increases, $e_{w,n}$ increases for a given value of St_n because higher lubrication pressures cause the glass transition to be reached with less penetration and a smaller fraction of the particle kinetic energy is lost. However, for $St_n < 1.0$ (medium-viscosity $St_n^* = 1.0$), where no glass-transition criterion is met and therefore the value of p_{gt} is irrelevant, the value of $e_{w,n}$ in this region is not sensitive to changes in viscosity. Again, the theory allows further insight into the mechanics of the collision. Specifically, velocity reversal for $St_n < St_n^*$ is due only to centrifugal forces. As viscosity increases, the collision velocity must also increase in proportion at fixed St_n, so that the penetration depth when the relative normal motion is arrested is unchanged. Similarly, the fractional recovery of the normal velocity when the particles separate is unchanged, and so $e_{w,n}$ is left unaffected by changes in viscosity.

In figures 9(*c*) and 9(*d*), θ_R is plotted against St_n using the experimental data and theoretical predictions, respectively, again for cases with differing viscosities. For $St_n > 2.0$ (low-viscosity $St_n^* = 2.0$), θ_R decreases as viscosity increases for a given St_n because the glass transition is reached more quickly. However, for $St_n < 1.0$ (high-viscosity $St_n^* = 1.0$), no glass transition is predicted to occur and θ_R is essentially unaffected by changes in viscosity at fixed St_n. Again, higher viscosity requires higher impact velocity at fixed St_n. The resulting increase in rotational velocity is offset by a proportional decrease in collision duration due to the increased centrifugal force. The theory agrees well with the observed trends; however, a quantitative mismatch is observed for $St_n < St_n^*$.

4.3. *Effects of liquid-layer thickness*

Figure 10 shows experimental data (figure 10*a*) and corresponding theoretical predictions (figure 10*b*) for $e_{w,n}$ for two cases with different thicknesses of the liquid coating, namely $\mu_{med_}x_{0,med_}ss_a_{large}$ and $\mu_{med_}x_{0,large_}ss_a_{large}$. For both the experiments and theory, St_n^* increases as the coating thickness increases. When $St_n < 1.0$ (thin-layer $St_n^* = 1.0$), no obvious difference is observed in the experimental values of $e_{w,n}$ as the coating thickness is changed, and likewise only very minor differences are observed in the theory. The energy lost to viscous dissipation to bring relative normal motion to rest is independent of the fluid-layer thickness, and so the viscous losses as the particles subsequently separate due to centrifugal forces are also nearly independent of the layer thickness, so $e_{w,n}$ is nearly independent of x_0 when St_n is less than the thin-layer St_n^*. Conversely, for $St_n > 1.4$ (thick-layer $St_n^* = 1.4$), more viscous dissipation occurs for the larger coating thickness as the separation between the surfaces decreases to the critical gap value specified by the dominant reversal criterion, and then increases again after reversal, and so $e_{w,n}$ decreases with increasing x_0.

In figures 10(*c*) and 10(*d*), θ_R is plotted against St_n for experimental results and theoretical predictions, respectively. Only small changes in θ_R are observed for St_n less than the thin-layer St_n^*, since the angular velocity is not sensitive to coating thickness (equation (3.10)), and the collision duration is approximately the same. In contrast, for St_n greater than the thick-layer St_n^*, as coating thickness increases, the particles must penetrate a larger distance during approach and reversal, so the collision duration increases, which results in an increase in θ_R in both experiment and theoretical predictions. The theory continues to predict the experimentally observed trends, but a quantitative mismatch is again observed for $St_n < St_n^*$.

https://doi.org/10.1017/jfm.2012.297 Published online by Cambridge University Press

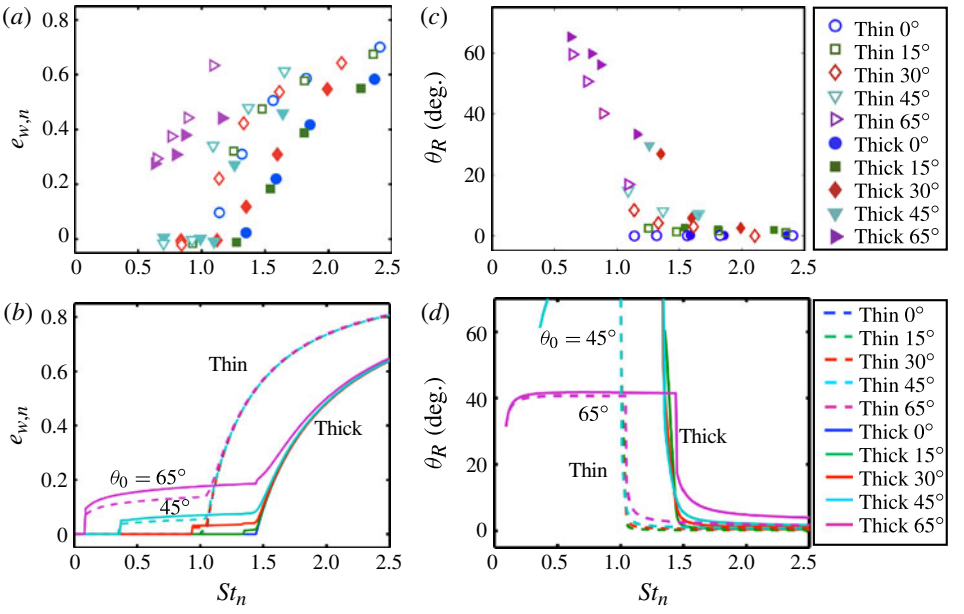


FIGURE 10. (Colour online) Normal restitution coefficient from (*a*) experiment and (*b*) theory, and rotation angle from (*c*) experiment and (*d*) theory as the coating thickness is increased from 270 μm (open symbols, dashed curves) to 420 μm (closed symbols, solid curves) for cases $\mu_{med}_x_{0,med}_ss_a_{large}$ and $\mu_{med}_x_{0,large}_ss_a_{large}$.

4.4. *Effect of particle size*

Finally, figure 11 shows the effect of particle radius on $e_{w,n}$ and θ_R for the cases $\mu_{med}_x_{0,med}_cs_a_{small}$ and $\mu_{med}_x_{0,med}_cs_a_{large}$. Here, particle material density is held constant so that particle mass also increases with radius. In figures 11(*a*) and 11(*b*), $e_{w,n}$ is plotted against St_n for the experimental results and theoretical predictions, respectively. The value of St_n^* remains constant as particle radius increases for both experiment and theoretical predictions. Furthermore, over the entire range of St_n for de-agglomerating collisions ($St_n > 1.1$), the values of $e_{w,n}$ remain constant as particle radius increases for both experiment and theoretical predictions (within experimental error). Since figure 11(*a*,*b*) is plotted in terms of St_n, which takes into account the changes in particle inertia and fluid resistance with changes in particle radius, the curves associated with the different radii collapse for $St_n > St_n^*$. For $St_n < St_n^*$, the theory predicts a decrease in $e_{w,n}$ with an increase in radius. This change is due to the balance of lubrication and centrifugal forces in (3.8), with v_n decreasing in proportion to $1/a^2$ (equation (3.3)).

In figures 11(*c*) and 11(*d*), θ_R is plotted against St_n for experimental results and theoretical predictions, respectively, for systems with different particle radii. Again, plotting θ_R versus St_n causes the curves associated with the different radii to nearly collapse for $St_n > St_n^*$. However, for $St_n < St_n^*$, a decrease in θ_R as particle radius increases is observed in both experiment and theoretical predictions. This decrease is due to string tension. As seen in (3.6), string tension increases with particle radius, so that the larger particles are slowed down more and do not rotate as far.

https://doi.org/10.1017/jfm.2012.297 Published online by Cambridge University Press

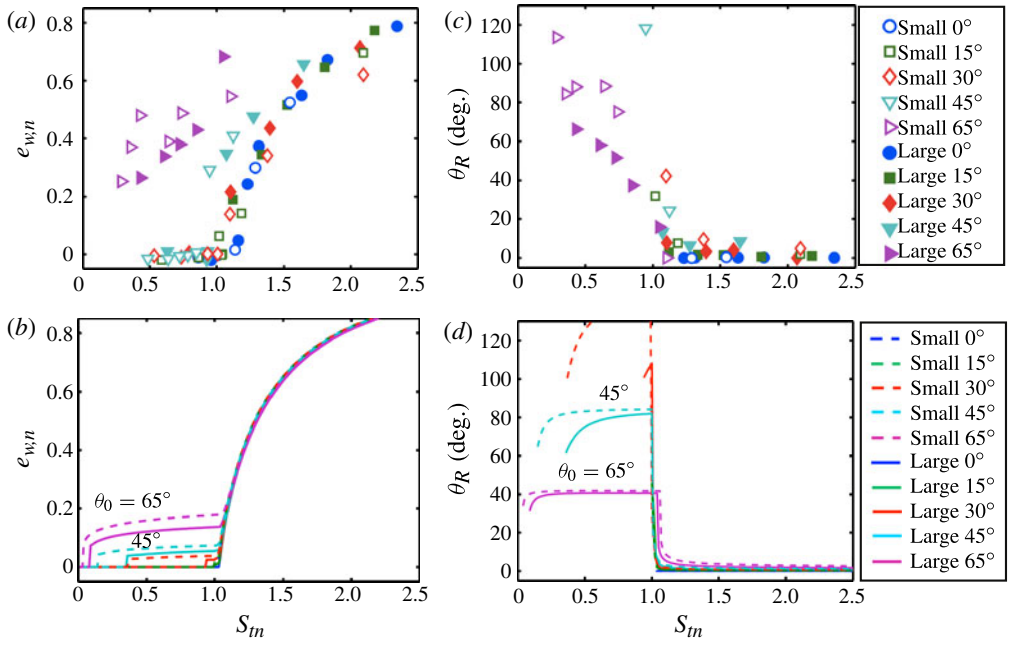


FIGURE 11. (Colour online) Normal restitution coefficient from (*a*) experiment and (*b*) theory, and rotation angle from (*c*) experiment and (*d*) theory as the radius is increased from 7.9 mm (open symbols, dashed curves) to 12.7 mm (closed symbols, solid curves) for cases $\mu_{med}_x_{0,med}_cs_a_{small}$ and $\mu_{med}_x_{0,med}_cs_a_{large}$.

4.5. *Summary of results*

The trends are summarized in table 2 for all of the parameters discussed. The theory consistently predicts the observed trends in $e_{w,n}$ and θ_R, which supports the physical interpretation of the experimental results presented in this work. For most parameters, different trends are observed for $St_n < St_n^*$ (stick–rotate–separate) than for $St_n > St_n^*$ (bounce), since different mechanisms are responsible for de-agglomeration.

5. Concluding remarks

Unlike previous efforts on wetted collisions, which focused on normal particle–particle collisions and normal and oblique particle–wall collisions, the focus of this work is on oblique collisions between two particles. In this system, the wetted particles can agglomerate and rotate as a doublet, so that centrifugal forces play a role in the dynamics. To better understand the interplay between the underlying physical mechanisms, a theory developed in Donahue *et al.* (2012) is used with a combination of experiments and lubrication (low-Reynolds-number) theory. In this work, the parameter space of the collisions is extended to include changes in viscosity, coating thickness, particle material, and particle radius. The theory consistently predicts the experimentally observed trends in the wetted restitution coefficient ($e_{w,n}$) and the angle that the agglomerate rotates during the collision (θ_R) as parameters are changed. Surprisingly, the trends are different depending on whether de-agglomeration occurs for values of St_n less than St_n^* or greater than St_n^*, the value of the Stokes number at which normal (head-on) collisions transition from stick to

https://doi.org/10.1017/jfm.2012.297 Published online by Cambridge University Press

	For $St_n < St_n^*$	For $St_n > St_n^*$	Figure
As $e_{dry} \uparrow$, $e_{w,n}$	$\leftrightarrow$ (Experiment) $\leftrightarrow$ (Theory)	$\uparrow$ (Experiment) $\uparrow$ (Theory)	8
As $e_{dry} \uparrow$, θ_R	$\leftrightarrow$ (Experiment) $\leftrightarrow$ (Theory)	$\leftrightarrow$ (Experiment) $\leftrightarrow$ (Theory)	8
As $\mu \uparrow$, $e_{w,n}$	$\leftrightarrow$ (Experiment) $\leftrightarrow$ (Theory)	$\uparrow$ (Experiment) $\uparrow$ (Theory)	9
As $\mu \uparrow$, θ_R	$\leftrightarrow$ (Experiment) $\leftrightarrow$ (Theory)	$\downarrow$ (Experiment) $\downarrow$ (Theory)	9
As $x_0 \uparrow$, $e_{w,n}$	$\leftrightarrow$ (Experiment) $\leftrightarrow$ (Theory)	$\downarrow$ (Experiment) $\downarrow$ (Theory)	10
As $x_0 \uparrow$, θ_R	$\leftrightarrow$ (Experiment) $\leftrightarrow$ (Theory)	$\uparrow$ (Experiment) $\uparrow$ (Theory)	10
As $a \uparrow$, $e_{w,n}$	$\downarrow$ (Experiment) $\downarrow$ (Theory)	$\leftrightarrow$ (Experiment) $\leftrightarrow$ (Theory)	11
As $a \uparrow$, θ_R	$\downarrow$ (Experiment) $\downarrow$ (Theory)	$\leftrightarrow$ (Experiment) $\leftrightarrow$ (Theory)	11

TABLE 2. Summary of trends of $e_{w,n}$ and θ_R at fixed St_n ($\uparrow$ increase, $\downarrow$ decrease, $\leftrightarrow$ no or small change).

bounce. Since the collision dynamics and de-agglomeration are primarily influenced by the particle deformation and reversal criteria associated with normal collisions when $St_n > St_n^*$, the same trends are observed here as in previous normal particle–particle collisions (Donahue *et al.* 2010*b*). However, centrifugal forces, which dominate the de-agglomeration process for $St_n < St_n^*$, do not have the same dependence on the experimental parameters; accordingly, the values of $e_{w,n}$ and θ_R are not very sensitive to any of the parameters varied for both experiment and theory predictions (within experimental error). Therefore, the resulting trends for $e_{w,n}$ and θ_R are different when $St_n < St_n^*$ than when $St_n > St_n^*$ (as summarized in table 2). Furthermore, while the pendulum strings affect the St_n at which agglomeration occurs, they do not affect significantly the values of $e_{w,n}$ and θ_R for the outcomes stick–rotate–separate and bounce; thus, strings do not affect a majority of the trends found, except for one – the effect of particle radius on θ_R.

In this work, a micro-level (particle-level) approach has been taken to study the collisions between wetted particles. Such work is crucial to understanding macro-level behaviour of many-particle systems, since collisions between particles in such systems are typically oblique. In descriptions of many-particle systems, normal collisions alone are not sufficient to describe the trends of bulk flow when input parameters are varied, since collisions that reverse direction due to centrifugal forces exhibit consistently different trends. Furthermore, the work here, together with previous work on oblique particle–wall collisions and normal collisions between more than two particles, provides the foundation for discrete element method (DEM) simulations of many-particle systems (Barnocky & Davis 1988; Kantak & Davis 2004; Donahue *et al.* 2010*b*). Additionally, the surprising influence of centrifugal forces on de-agglomeration is expected to lead to the development of better population balance (continuum) models that more accurately take into account oblique collisions.

https://doi.org/10.1017/jfm.2012.297 Published online by Cambridge University Press

Acknowledgements

The authors are grateful for the funding support for this work provided by the National Science Foundation (CBET 0754825 and a REU supplement).

REFERENCES

BARNOCKY, G. & DAVIS, R. H. 1988 Elastohydrodynamic collision and rebound of spheres – experimental-verification. *Phys. Fluids* **31**, 1324–1329.

BARNOCKY, G. & DAVIS, R. H. 1989 The influence of pressure-dependent density and viscosity on the elastohydrodynamic collision and rebound of two spheres. *J. Fluid Mech.* **209**, 501–519.

CHAUDHURI, B., MEHROTRA, A., MUZZIO, F. J. & TOMASSONE, M. S. 2006 Cohesive effects in powder mixing in a tumbling blender. *Powder Technol.* **165**, 105–114.

CROSS, N. L. & PICKNETT, R. G. 1968 Comment on paper effect of capillary liquid on force of adhesion between spherical solid particles. *J. Colloid Interface Sci.* **26**, 247–249.

DAVIS, R. H. 1987 Elastohydrodynamic collisions of particles. *Physico-Chem. Hydrodyn.* **9**, 41–52.

DAVIS, R. H., RAGER, D. A. & GOOD, B. T. 2002 Elastohydrodynamic rebound of spheres from coated surfaces. *J. Fluid Mech.* **468**, 107–119.

DAVIS, R. H., SERAYSSOL, J. M. & HINCH, E. J. 1986 The elastohydrodynamic collision of two spheres. *J. Fluid Mech.* **163**, 479–497.

DONAHUE, C. M., DAVIS, R. H., KANTAK, A. A. & HRENYA, C. M. 2012 Mechanisms for agglomeration and deagglomeration following oblique collisions of wetted particles. *Phys. Rev.* E (submitted).

DONAHUE, C. M., HRENYA, C. M. & DAVIS, R. H. 2010*a* Stokes's cradle: Newton's cradle with liquid coating. *Phys. Rev. Lett.* **105**, 34501.

DONAHUE, C. M., HRENYA, C. M., DAVIS, R. H., NAKAGAWA, K. J., ZELINSKAYA, A. P. & JOSEPH, G. G. 2010*b* Stokes' cradle: normal three-body collisions between wetted particles. *J. Fluid Mech.* **650**, 479–504.

ENNIS, B. J., TARDOS, G. & PFEFFER, R. 1991 A microlevel-based characterization of granulation phenomena. *Powder Technol.* **65**, 257–272.

FISHER, R. A. 1926 On the capillary forces in an ideal soil; correction of formulae given by W. B. Haines. *J. Agric. Sci.* **16**, 492–505.

GONDRET, P., LANCE, M. & PETIT, L. 2002 Bouncing motion of spherical particles in fluids. *Phys. Fluids* **14**, 643–652.

IVESON, S. M. 2002 Limitations of one-dimensional population balance models of wet granulation processes. *Powder Technol.* **124**, 219–229.

JOSEPH, G. G., ZENIT, R., HUNT, M. L. & ROSENWINKEL, A. M. 2001 Particle–wall collisions in a viscous fluid. *J. Fluid Mech.* **433**, 329–346.

KANTAK, A. A. & DAVIS, R. H. 2004 Oblique collisions and rebound of spheres from a wetted surface. *J. Fluid Mech.* **509**, 63–81.

KANTAK, A. A. & DAVIS, R. H. 2006 Elastohydrodynamic theory for wet oblique collisions. *Powder Technol.* **168**, 42–52.

KANTAK, A. A., HRENYA, C. M. & DAVIS, R. H. 2009 Initial rates of aggregation for dilute, granular flows of wet particles. *Phys. Fluids* **21**, 023301.

LEKHAL, A., CONWAY, S. L., GLASSER, B. J. & KHINAST, J. G. 2006 Characterization of granular flow of wet solids in a bladed mixer. *AIChE J.* **52** (8), 2757–2766.

LI, H. M. & MCCARTHY, J. J. 2005 Phase diagrams for cohesive particle mixing and segregation. *Phys. Rev.* E **71**, 021305-1–021305-8.

LIAN, G., ADAMS, M. & THORNTON, C. 1996 Elastohydrodynamic collisions of solid spheres. *J. Fluid Mech.* **311**, 141–152.

LIAN, G. P., THORNTON, C. & ADAMS, M. J. 1993 A theoretical study of the liquid bridge forces between two rigid spherical bodies. *J. Colloid Interface Sci.* **161**, 138–147.

LIU, P. Y., YANG, R. Y. & YU, A. B. 2011 Dynamics of wet particles in rotating drums: effect of liquid surface tension. *Phys. Fluids* **23**, 013304.

https://doi.org/10.1017/jfm.2012.297 Published online by Cambridge University Press

MARSTON, J., WONG, W. & THORODDSEN, S. 2010 Direct verification of the lubrication force on a sphere travelling through a viscous film upon approach to a solid wall. *J. Fluid Mech.* **655**, 515–526.

MASON, G. & CLARK, W. C. 1965 Liquid bridges between spheres. *Chem. Engng Sci.* **20**, 859–866.

MIKAMI, T., KAMIYA, H. & HORIO, M. 1998 Numerical simulation of cohesive powder behaviour in a fluidized bed. *Chem. Engng Sci.* **53**, 1927–1940.

O'NEILL, M. E. & MAJUMDAR, R. 1970 Asymmetrical slow viscous fluid motions caused by the translation or rotation of two spheres. Part I. The determination of exact solutions for any values of the ratio of radii and separation parameters. *Z. Angew. Math. Phys.* **21**, 164–179.

SAITOH, K., BODROVA, A., HAYAKAWA, H. & BRILLIANTOV, N. V. 2010 Negative normal restitution coefficient found in simulation of nanocluster collisions. *Phys. Rev. Lett.* **105**, 238001.

SALCUDEAN, M., DARABI, P., POUGATCH, K. & GRECOV, D. 2009 A novel coalescence model for binary collision of identical wet particles. *Chem. Engng Sci.* **64**, 1868–1876.

TALU, I., TARDOS, G. I. & KHAN, M. I. 2000 Computer simulation of wet granulation. *Powder Technol.* **110**, 59–75.

WEBER, M. W. & HRENYA, C. M. 2006 Square-well model for cohesion in fluidized beds. *Chem. Engng Sci.* **61**, 4511–4527.

XU, Q., ORPE, A. V. & KUDROLLI, A. 2007 Lubrication effects on the flow of wet granular materials. *Phys. Rev.* E **76**, 31302.

https://doi.org/10.1017/jfm.2012.297 Published online by Cambridge University Press